IMPACT OF MAGNETOHYDRODYNAMIC (MHD) INDUCED DRAG ON HIGH BALLISTIC COEFFICIENT AEROCAPTURE AT NEPTUNE

David R. Komar,[*] Justin Green,[†] and Dr. Bob Moses[‡]

This paper presents analyses illustrating the benefits of magnetohydrodynamic (MHD) drag force control for a capsule performing aerocapture at Neptune relative to the same capsule utilizing conventional aerodynamic-only control across a range of design and flight conditions. MHD technology utilizes an onboard magnet to create a magnetic field that interacts with the ionized plasma surrounding the capsule at hypersonic velocities, thus creating an electron current and inducing a Lorentz force used to increase capsule drag. The study assumes a 4.57-meter Mars Science Laboratory (MSL) 70-degree sphere-cone capsule aerodynamic shape arrives hyperbolically at Neptune and aerocaptures into a synchronous Triton orbit (3986 km x 430,000 km orbit inclined 157 degrees) that offers repeated flyby opportunities. Hyperbolic arrival velocity and the capsule entry mass (i.e., ballistic coefficient) are varied over a wide range of values to study the impact of these variables on key flight performance and sizing parameters. Results show reduced heat rates, heat loads, and thermal protection system mass for MHD cases at all conditions, with the benefit of MHD relative to conventional aerodynamic-only options increasing as ballistic coefficient increases, suggesting the payoff for MHD is significantly better for high-mass entry system design concepts with high ballistic coefficients.

INTRODUCTION

Ionized plasma flows occurring around objects at high velocities have been studied since the 1950s.[1,2] Borrowing from terrestrial electrical power generation, an ionized (and electrically conductive) flow in a tube when exposed to a magnetic field creates an electrical current in a wire. This power generation practice is known as magnetohydrodynamics (MHD). An electromotive force is also created that acts on the flow field as well as the magnet. Borrowing from this terrestrial analog, for a spacecraft entering an atmosphere at hypersonic speeds, the resulting ionized flow when electrically conductive and in the presence of a magnetic field generates an electrical current in a wire to harvest electrical power as well as produces electromagnetic forces that can be used to control the spacecraft.

The application of MHD to induce a drag-only force on an entering spacecraft is illustrated in Figure 1. Hypersonic entry produces an ionized plasma surrounding the spacecraft. With an

[*] Aerospace Technologist, Vehicle Analysis Branch, NASA Langley Research Center, Hampton, VA 23681, USA.
[†] Aerospace Technologist, Atmospheric Flight and Entry Systems Branch, NASA Langley Research Center, Hampton, VA 23681, USA.
[‡‡] Independent Contractor, formerly from NASA Langley Research Center, Hampton, VA 23681, USA.

onboard magnet, a magnetic field, $\vec{B}$, can be applied on the plasma to create an electron current, $\vec{J}$, and induce a Lorentz force experienced by the charged particles in the plasma.

$$\vec{F}_{Lorentz} = \vec{J} \times \vec{B} \tag{1}$$

An equal and opposite force is imparted on the entry vehicle and assuming a uniform magnetic field and the spacecraft entering the atmosphere with zero angle-of-attack, the Lorentz forces act equally and oppositely on the vehicle in only the drag direction. These reactions integrated over the area of the magnet results in the MHD drag, $\vec{F}_{MHD\ Drag}$. This force is in addition to the aerodynamic forces. The current, I, to one centrally located or multiple concentrically located electromagnets can be manipulated to enable active control of the MHD induced drag.

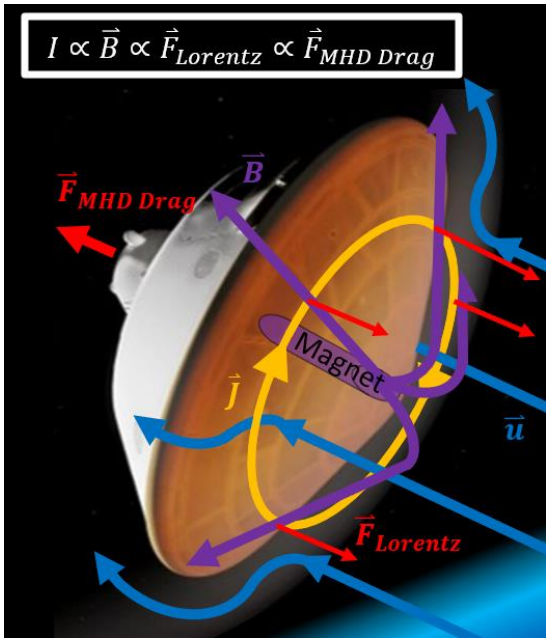

Figure 1. Magnetohydrodynamic Drag Force Control Illustration.

Since the early 2000s, studies have been conducted on the feasibility of MHD to benefit missions to Mars, Venus, Neptune, and return to Earth.[3-15] These studies have depended primarily on numerical analysis using codes created for modeling the ionized conductive flow field around the entering spacecraft during its interaction with the magnetic field extending from the forebody of the spacecraft. During that same timeframe, NASA Langley Research Center (LaRC) has been working diligently via fundamental research projects, NASA Innovative Advanced Concepts (NIAC) studies, NASA Center Innovation Fund (CIF), NASA Space Technology Graduate Research Opportunities (NSTGRO), and other funded studies to mature the simulation capabilities for MHD entry, descent, and landing (EDL) and aerocapture at destinations with atmospheres. Those studies have advanced our simulation capabilities and modeling tools in computational fluid dynamics (CFD), MHD, and flight mechanics.

The latest application of those new tools, as presented in this paper, explores the sensitivities on heat loads, heat rates, and thermal protection system (TPS) mass for a spacecraft performing aerocapture at Neptune over a range of entry masses (i.e., ballistic coefficients) and hyperbolic arrival velocities. Results for cases using MHD induced drag force control are compared to those

of a capsule using conventional aerodynamic-only aerocapture control, specifically bank angle modulation (BAM). BAM is a control concept whereby the lift vector produced by the spacecraft at a fixed, non-zero angle of attack is rotated (banked) about the velocity vector of the capsule to guide its trajectory through atmospheric entry to exit. Direct force control (DFC) and drag modulation (DM) are two additional aerodynamic-only control concepts that could be considered. DFC uses a combination of angle of attack and side-slip angle modulation to control both the downrange and crossrange trajectory.[16] DM uses either a jettisonable drag area or a continuously variable (morphing) geometry to control the downrange trajectory.[17] However, as discussed later, given the breadth of cases evaluated and the fact that our goal is a relative assessment of MHD compared to aerodynamic-only control concepts, unguided (open-loop) trajectories are flown in this study. As such, the differences in BAM, DFC, and DM observed when utilizing guided (closed-loop) control strategies are not investigated herein.

BACKGROUND

The current understanding on MHD EDL stems from work that began in the 1950s and continues today. Resler and Sears showed interest in MHD for aerodynamics (magnetoaerodynamics) throughout 1960s.[1] Zeimer and Bush (1958) performed experimental investigations on spheres to assess increases in standoff distances of bow shocks.[2] Meyer (1958) studied reducing aerodynamic heat-transfer rates by magnetohydrodynamic techniques.[18] Numerous other analytical estimations and approximations occurred during the 1960s, but no results for full-scale experiments are found in the literature. There was very little new research published on this topic for decades. Numerical investigations by Poggie and Gaitonde of the Air Force Research Laboratory (AFRL) in 2000-2002 compares well to early analytical and experimental measurements for shock standoff distance.[19] Macheret et al. (2004) performed calculations to determine power available through MHD energy generation over a full trajectory.[20] Moses (2005) at NASA LaRC showed how MHD could generate power, collect oxygen, and generate Lorentz forces during entries at Mars.[3,4] Fujino (2008, 2009) performed a full-field numerical flow field and trajectory dynamics simulation for Earth entry.[5,6] Kim and Boyd (2012) performed MHD-CFD simulations of the Mars Pathfinder entry vehicle forebody with an applied magnetic field, recording an increase in drag and decrease in convective heat flux.[7] In collaboration with NASA LaRC, Ali (2018, 2019) extended upon Moses' research in power and drag force generation at Mars.[8,9] Moses et al. (2022) provided initial power generation and Lorentz force estimates of a patch MHD aerocapture system for entries at Neptune, Mars, and Earth and illustrated the application of a new stepwise simulation capability for estimating performance of MHD aerocapture for destinations with atmospheres.[10] Parent et al. (2022, 2024) illustrated a series of improvements in computational capabilities using a combined MHD-CFD solver called CFDWARP to estimate power generation and Lorentz forces for hypersonic entries at Earth and other destinations with atmospheres.[11,12] Parent et al. (2024) provided a comparison of performance when using two electrodes and electrodeless MHD concepts. Fawley et al. (2024) compared entries at Mars and Venus to illustrate the differences in benefits when using MHD at these destinations.[15] There are other pockets of research exploring the effects of magnetic forces on ionized conductive plasma around spacecraft entering Earth or Mars, such as Gülhan (2009), Kawamura et al. (2009, 2013), Bisek (2010), Gildfind et al. (2018, 2022), and Smith (2020).[21-27]

Nguyen et al. (2022, 2024) used the Program to Optimize Simulated Trajectories – II (POST2), a flight mechanics code developed by NASA LaRC, to compare MHD drag modulation to the aerodynamic-only BAM, DFC, and DM applied to aerocapture at Neptune.[13,14] These investigations looked at both open-loop and closed-loop control of a spacecraft and led to several key findings:

1) The increased deceleration capability offered by MHD can be traded for decelerating more mass (more payload) and enabling faster hyperbolic arrival velocities (Vinf).

2) MHD offers deceleration earlier in the trajectory as compared to aerodynamic-only. This combined with increased deceleration forces leads to less penetration into the atmosphere and a lower aerodynamic heating environment.
3) MHD does not require ballast, jettison events, aerodynamic flaps, or complex size-changing aeroshell mechanisms.[10]

The results from Nguyen et al. motivated and directly fed into the study discussed herein. Of particular interest is the performance benefits offered by MHD, relative to aerodynamic-only strategies, over a range of Vinf and spacecraft masses. These parameters have direct impacts on the interplanetary transit times and on the class of spacecraft that can benefit from MHD technology.

ANALYSIS APPROACH AND METHODS

Analysis Approach

Building on the knowledge gained from previous studies, our hypothesis is that the relative benefits for MHD increase with increased entry velocity and entry mass (i.e., ballistic coefficient). As such, the objective of this effort was to quantify the benefits of MHD relative to aerodynamic-only approaches over a range of hyperbolic arrival velocities and spacecraft ballistic coefficients.

A two-part approach was used for the technical analysis.

First, a *Relative Flight Performance Assessment* of MHD versus aerodynamic-only across a range of arrival flight conditions and entry masses is performed. Results are illustrated in contour plots showing the variation in key trajectory and heating parameters over the range of arrival velocities and entry masses. Contours are produced for the MHD drag modulated cases, aerodynamic-only cases, as well as MHD relative to aerodynamic-only.

Second, for a select set of cases, we conduct *Aeroheating and TPS Sizing Analyses* to quantify the TPS mass impact of MHD relative to aerodynamic-only. Results for this analysis are stacked bar charts comparing appropriate TPS options applied to MHD and aerodynamic-only trajectories over a range of entry masses and hyperbolic arrival Vinf.

Key assumptions used in the study include:

- Aerodynamic shape assumes a fixed, 4.57-meter diameter, 70-degree sphere-cone capsule spacecraft similar to the Mars Science Laboratory (MSL).
- Neptune target orbit assumes a 3986 km x 430,000 km orbit inclined 157 degrees that offers repeating Triton flybys.
- While several aerodynamic-only approaches could be considered, including bank angle modulated (BAM), direct force control (DFC), and drag modulated (DM), only BAM is assessed for the comparison with MHD drag modulation.

One of the key benefits of MHD, known from prior works, is that the heating environment experienced by an MHD controlled spacecraft is more benign than for an aerodynamic-only controlled spacecraft at the same entry velocity and entry mass. Thus, for a given/fixed entry mass, those benefits could be realized by either: 1) increasing scientific payload mass due to reductions in TPS mass; or 2) increasing arrival speeds with corresponding shorter interplanetary transit times for a given payload and TPS mass.

In general, this study's primary goal was to quantify the TPS mass savings as the primary metric, leaving the quantification of the relative interplanetary flight time savings MHD-based aerocapture offers as a function of arrival velocity for future work. However, to establish a viable range of hyperbolic arrival velocities for use in our study, previous work from Noca and Bailey (2004) was

consulted, resulting in the selection of an arrival Vinf ranging from 17.5 km/s to 23.5 km/s. This corresponds to an inertial entry velocity of 29 km/s to 33 km/s at Neptune and a ballistic gravity assist trajectory flight time ranging from 12 years to 8 years.[28]

Entry mass (as opposed to ballistic coefficient) was chosen as the second independent variable to simplify the execution of both MHD and BAM cases. Note, however, the drag coefficient for MHD is 20% higher than BAM cases at the same entry mass since it nominally operates at zero angle of attack (see Table 1). Thus, at the same entry mass, the ballistic coefficient is 20% lower for MHD compared to BAM. To support the development of trajectory contour plots, a range of 1 to 5 metric tons entry mass was selected. This corresponds to a ballistic coefficient range of 36 to 179 kg/m^2 for MHD cases and 45 to 224 kg/m^2 for BAM. However, for the *Aeroheating and TPS Sizing Analyses* cases, this entry mass range was extended up in steps of 5 t to a maximum of 20 t (corresponding to an upper limit on ballistic coefficient of 716 kg/m^2 for MHD and 898 kg/m^2 for BAM).

Analysis Tools and Methods

This sub-section provides an overview of the tools and methods used in this study, along with some of the key study assumptions used for each discipline. Figure 2 provides a graphical summary of some of the MHD-specific capabilities employed in this study, but a more verbose description is provided below for each discipline, including those required to support analysis of BAM aerodynamic-only cases.

LAURA	CFDWARP	POST2	FIAT
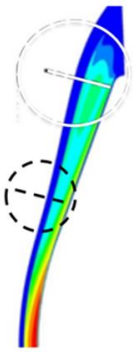	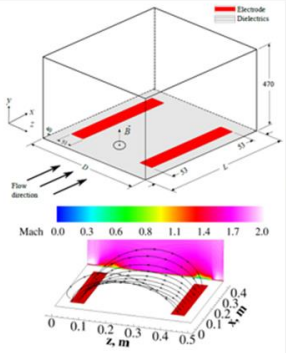	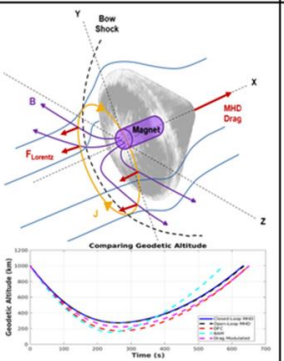	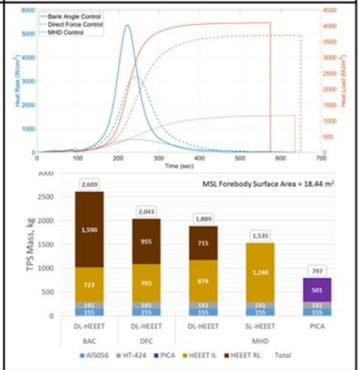
Conduct aero-heating analysis to select places of ionization and flow velocity for MHD system analysis	Port LAURA results into CFDWARP to calculate electrical and thermal conductivities of ionized flow for sizing MHD patch system and calculating Lorentz forces needed for controls analysis	Port results from LAURA and CFDWARP into POST2 for calculating entry trajectories and comparing MHD control results with other aerodynamic control strategies	Utilize trajectory information from POST2 to calculate heat rates and heat loads on the spacecraft and size the Thermal Protection System based on known properties of materials such as HEEET and PICA

Figure 2. Disciplinary Approach for Assessing MHD Concepts.

Aerodynamics. Utilization of the MSL aerodynamic shape allowed use of an existing, validated aerodynamic database embedded in and called directly from the trajectory performance tool. Given that unguided (open-loop) and undispersed trajectories were used to support the relative analyses performed and presented herein, only nominal drag and lift coefficients were required for the selected angles of attack flown for MHD and BAM cases (see Table 1).

Aerothermodynamics and Magnetohydrodynamics. Aerothermal and MHD-specific flow field analyses were performed to develop the necessary databases using a combination of the NASA Langley Aerothermodynamic Upwind Relaxation Algorithm (LAURA), the Hypersonic Air Radiation Algorithm (HARA), and the University of Arizona CFDWARP software.[29,30] This included a capsule stagnation point aerothermal database valid over the range of Neptune hyperbolic arrival velocities (17.5 to 23.5 km/s) and entry masses (1 to 20 t) considered in this study.

Radiative heating data was used to develop a useful correlation that predicts radiative heat rate as a function of post-shock equilibrium temperature and density:

$$\boldsymbol{Q_{rad} = 5.1025 \cdot 10^{-44} \cdot T^{12.0857} \cdot \rho^{0.8474}} \quad (2)$$

where T (in Kelvin) and ρ (in kg/m^3) are the temperature and density downstream of the normal shock at a given freestream flight condition, and Q_{rad} is in W/cm^2.

Convective heating data compared favorably to results from the Sutton-Graves equation[31]. As such, the Sutton-Graves equation was utilized to predict convective heating at the stagnation point across all flight conditions to support both the *Relative Flight Performance Assessment* and the *Aeroheating and TPS Sizing Analyses*. The MSL capsule physical nose radius of 1.125 meters was used for the effective nose radius.

Electron number density, electron temperature, and gas number densities directly govern the electrical conductivity of the plasma near the vehicle. The electrical conductivity of the plasma is directly proportional to the electrical current in Equation (1). LAURA CFD on a hemisphere in a Neptune relevant atmosphere was used to generate relationships for these quantities relative to atmospheric density and freestream velocity. Values along the stagnation line were used to build a multivariable lookup table based on freestream velocities between 16 to 32 km/s and atmospheric densities between 10^{-3} and 10^{-6} kg/m^3. A limited number of LAURA solutions were available, so values were extrapolated for atmospheric density between 10^{-6} and 10^{-10} kg/m^3, and electrical conductivity was assumed to be zero for any density below 10^{-10} kg/m^3. Computing values at these lower densities requires rarefied flow simulations, which requires a direct simulation Monte Carlo solver instead of Navier-Stokes.[13]

Flight Mechanics. All aerocapture trajectory analyses are performed using the Program to Optimize Simulated Trajectories (POST2).[32] Given the breadth of the desired trades and analyses this effort utilizes, unguided (open-loop) and undispersed trajectories are flown to enable a consistently executed assessment that clearly reveals the relative differences and trends. In addition, the aeroheating environment required to support TPS sizing is not substantially different for guided versus nominal unguided trajectories.[13,14]

Assessments of MHD and BAM trajectory cases utilize the same process that includes first determining the entry corridor/window by finding the steepest and shallowest trajectories that hit the orbital apoapsis, and then performing a nominal trajectory within that window for comparison to other cases and quantification of a nominal aeroheating environment. For both MHD and BAM cases, a Matlab script is used to drive a bisection process that determines the entry flight path angle (FPA) that hits the target apoapsis altitude of 430,000 km.

Table 1 summarizes the assumptions used in the unguided trajectories for both MHD and BAM. Note that since the drag coefficient for MHD cases is 20% higher than for BAM cases, at a given entry mass the ballistic coefficient for MHD cases is 20% lower than BAM cases. To some degree this influences the results shown in the contour plots below, although not enough to account for all the observed improvement in the MHD cases.

For BAM cases, angle of attack is fixed at -20 deg. Steep cases assume lift-down (bank angle = 0 deg) at entry interface (EI). This orientation is held fixed until atmospheric exit and requires a steeper entry FPA to hit the target apoapsis. Likewise, the shallow cases assume a lift-up (bank angle = 180 deg) from EI to atmospheric exit, and the resulting entry FPA represents the shallowest angle that can still hit the apoapsis target. The difference in these FPAs represents the theoretical entry corridor or window, with larger delta-FPAs being desirable. Finally, for each BAM case, a nominal trajectory is flown assuming lift-down (bank angle = 0 deg) from EI to periapsis. At periapsis the lift vector is flipped to lift-up orientation (bank angle = 180 deg) and held until atmospheric exit.

Table 1. Summary of POST2 Assumptions for Unguided (Open-Loop) Aerocapture Trajectories.

Case	BAM	MHD
Angle of Attack	-20 deg	0 deg
Drag Coefficient	1.358	1.704
Control Type	Bank Angle Modulation	Electromagnet Current
Steep		
EI to Periapsis	0 deg	20 Amps
Periapsis to Exit	0 deg	20 Amps
Shallow		
EI to Periapsis	180 deg	180 Amps
Periapsis to Exit	180 deg	180 Amps
Nominal		
EI to Periapsis	0 deg	100 Amps
Periapsis to Exit	180 deg	100 Amps

For MHD cases, angle of attack and bank angle are fixed a 0 deg. The entry corridor is determined by flying the steep and shallow trajectories at the minimum and maximum allowable currents supplied to the MHD electromagnet, respectively. For this study, the assumed minimum allowable current to the electromagnet is 20 amps, and the assumed maximum current is 180 amps. Current (and vehicle orientation) are held constant from EI to atmospheric exit, and the FPA is determined that hits the target apoapsis. With the entry corridor now determined, a nominal trajectory is flown with an assumed nominal electromagnet current of 100 amps, again held constant from EI to exit.

Aeroheating Analysis. In support of the *Relative Flight Performance Assessment*, the aeroheating profile along each trajectory is based solely on application of the Sutton-Graves equation for convective heating at the stagnation point. This enabled a consistent methodology to predict heating effects over the range of arrival velocity and entry mass considered. Effects of radiative heating are not included in the resulting maximum heat rate and total heat load results shown in the contour plots discussed in the Technical Results section.

In support of the *Aeroheating and TPS Sizing Analyses*, the aeroheating environments along the trajectory are first determined for all cases selected for TPS sizing. The Sutton-Graves equation was again used to estimate the convective heating at the stagnation point along the trajectory, while the correlation presented in the aerothermodynamics discipline overview was used to predict radiative heating at the stagnation point.

For each aeroheating and TPS sizing case analyzed, the aeroheating profile along the nominal trajectory at the spacecraft stagnation point was determined and written to environment files appropriate for input to the TPS sizing tool FIAT, discussed next.

TPS Sizing. In support of the *Aeroheating and TPS Sizing Analyses*, the Fully Implicit Ablation and Thermal Response Program (FIAT) was used to size the appropriate ablative TPS stackup options.[33] In addition to the aeroheating surface environment profile (including both convective and radiative heating) along the trajectory at the vehicle stagnation point, FIAT requires material properties data inputs for each TPS option considered. Material systems appropriate for Neptune aerocapture at the conditions considered in the study include two Phenolic Impregnated Carbon Ablator (PICA) TPS options and two Heatshield for Extreme Entry Environment Technology (HEEET) TPS options:

- Conformal PICA, or C-PICA,
- PICA domestic, or PICA-D,
- Single-layer HEEET, or SL-HEEET, also called three-dimensional mid-density carbon phenolic (3MDCP), and
- Dual-layer HEEET, or DL-HEEET.

PICA-D is a tiled TPS used recently on the Mars 2020 mission which is made of a carbon fiber preform impregnated with phenolic resin.[34] PICA-D is appropriate for use with maximum heat rates up to 2500 W/cm^2.

C-PICA is a less mature but more mass efficient option than PICA-D for heating rates below 1500 W/cm^2. Material properties for C-PICA, however, were not available to enable quantitative assessment, although C-PICA is discussed qualitatively.[35]

DL-HEEET is a dual-layer, 3D woven material that can be tailored to mission requirements. The outer recession layer (RL) is a dense weave of carbon fiber intended to handle the heat flux of atmospheric entry, while the inner insulation layer (IL) is a mid-density weave of blended carbon and phenolic yarn intended to handle the heat load of atmospheric entry. DL-HEEET is appropriate for use at maximum heat rates that exceed 3500 W/cm^2.[36-38]

3MDCP uses the IL of the DL-HEEET design in a single-layer TPS used for maximum heat rate applications up to 3500 W/cm^2. At these heat rates 3MDCP is more mass efficient than DL-HEEET, but at lower heat rates it is not as efficient as PICA-D or C-PICA.[36-37]

Key modeling assumptions used in FIAT for TPS sizing include:

- For maximum heat rates < 2500 W/cm^2, only PICA-D was evaluated.
- 3MDCP was evaluated for maximum heat rates between 2500 and 3500 W/cm^2, while only DL-HEEET was evaluated for cases exceeding 3500 W/cm^2.
- For all options the TPS was bonded to aluminum 2024 structure using HT-424 paste adhesive, and the TPS thickness optimization was based on limiting the maximum temperature to 760 degrees Rankine at the adhesive-to-structure interface layer.
- The surface energy balance for ablation option was used to estimate surface recession rate and thermal response through the thickness of each TPS system.
- The dynamic chemistry option was used, which solves equations for chemical equilibrium between the ablating surface, pyrolysis gas, and the Neptune atmosphere.
- A five (5) minute cooldown is assumed prior to jettison of the heat shield.

The TPS sizing process used the three (3) branch sizing process documented by Mahzari and Milos (2018) that was defined for sizing DL-HEEET and ensures sufficient margin is designed into

the TPS to protect against the many uncertainties in the trajectory flight path, heating environments, manufacturing, installation, and analytical modeling.[39] The three branch process was then adapted for the PICA-D and 3MDCP single layer TPS options.

MHD Electromagnet Sizing. While MHD cases benefit from decreased TPS mass relative to the BAM cases at the same arrival velocity and entry mass, MHD cases also require a system of electromagnets to establish the magnetic field and a control system to modulate the current to the magnet during flight.

Magnet sizing assumes a distributed set of magnets located around the nose of the heatshield.[40] Nguyen (2024) estimates that the total mass for a set of electromagnets distributed around the nose of the heatshield, designed to collectively provide a maximum magnetic field strength over 1.25 Telsa, is less than 150 kg.[14] Each electromagnet nominally draws approximately 100 Amperes of electrical current, with power drawn from the ionized plasma flow. However, an on-board power storage system (batteries, for example) could also be used as an alternative but would add additional mass.

TECHNICAL RESULTS

Relative Flight Performance Assessment. Initial analysis was performed to evaluate the trajectories and heating indicators over a range of arrival velocities and entry masses for both BAM and MHD options. Results are presented as contour plots in Figure 3 through Figure 14. The abscissa shows the arrival Vinf over the 17.5 km/s to 23.5 km/s range, while the ordinate shows the vehicle mass at entry over the 1000 kg to 5000 kg range. Contours are shown for maximum heating rate, total heat load, maximum deceleration, periapsis altitude, periapsis atmospheric density, time from EI to periapsis, time from EI to exit, entry corridor/window angle, and nominal entry flight path angle. Figure 8 plots the deceleration as a function of altitude for specific cases as discussed below.

In Figure 3 the maximum heat rate contour is shown for BAM cases, while Figure 4 shows the same contours for MHD cases. Figure 5 shows a contour of the relative difference in maximum heat rate (MHD minus BAM), which is the difference between the two contour plots shown in Figure 3 and Figure 4. Figure 5 illustrates how the relative benefit for MHD (i.e., decrease in maximum heat rate) increases as both entry mass and arrival velocity increase. A similar trend shown in Figure 6 for the relative difference (MHD minus BAM) heat load contour highlights how total heat load for MHD relative to BAM decreases as both arrival velocity and entry mass increase.

Figure 7 and Figure 10 through Figure 14 show additional relative difference (MHD minus BAM) contour plots. Figure 9 plots, for the atmospheric density at periapsis contour, the ratio (as opposed to the difference) of MHD to BAM. These relative plots were generated and included to further illustrate how the relative difference between MHD and BAM changes with increasing entry mass and arrival velocity.

Figure 7 shows MHD cases experience higher maximum (or peak) deceleration over most of the range of cases. The exception where BAM experiences higher peak deceleration is in the top left corner where the entry masses are on the high end of the range and the arrival velocities are on the low end of the range. Initially it was thought that the relative maximum deceleration contour would be sufficient to illustrate that MHD offered increased deceleration at high altitude conditions where aerodynamic drag is negligible. However, since the vehicle flight profile is a function of the deceleration profile, not just the peak deceleration, a comparison of specific cases is needed to confirm this hypothesis. Figure 8 was generated to compare BAM and MHD deceleration profiles, shown as a function of altitude, for the extreme cases in the contour plot (specifically, the top left and bottom right cases). As Figure 8 shows, regardless of the relative peak deceleration, the MHD

cases begin decelerating at higher altitudes before the BAM begins to encounter sufficient atmospheric density to decelerate aerodynamically. This comparison illustrates the deceleration advantage for MHD relative to BAM.

Figure 9 shows for all cases that the periapsis altitude is greater for MHD than BAM. As both arrival velocity and entry mass increase, the relative (MHD minus BAM) difference is decreasing. Consequently, as shown in Figure 10, as both arrival velocity and entry mass increase, the periapsis density ratio (i.e., density at periapsis for MHD divided by density at periapsis for BAM) is increasing.

As shown in Figure 11, it takes longer for MHD to get from EI to periapsis, but Figure 12 shows that the total EI to exit atmospheric flight time is shorter for MHD. This is because MHD can decelerate at higher altitudes compared to BAM, so it takes longer to reach periapsis. However, since for MHD the periapsis altitude is higher and the periapsis velocity is lower, it takes less time for the remaining deceleration to target the required orbital velocity.

In Figure 13, we see the entry corridor (window) for MHD is smaller than for BAM. While this is not desirable, it is more due to the fact the MHD case is drag-modulated (DM) as opposed to being a characteristic of MHD. Deshmukh, Spencer, and Dutta (2022) showed that lifting trajectories have a much wider entry corridor than ballistic drag-modulated control strategies, even at lift-to-drag (L/D) ratios as low as 0.2.[17] Lift modulated MHD control strategies, not investigated in this study, are expected to have a larger entry corridor.

Finally, as shown in Figure 14, the nominal entry FPA is shallower for MHD (where the positive values on the relative contour represent MHD having a less negative FPA).

In summary, from these plots we observe MHD induced drag cases, relative to BAM aerodynamic-only cases, experience increased deceleration at higher altitudes, lower entry FPA, higher altitude at periapsis, lower velocity at periapsis, longer flight time to periapsis, and longer overall flight time. This leads to lower maximum heat rate and lower total heat load, with the benefits for MHD increasing as arrival Vinf and entry mass (i.e., ballistic coefficient) increase.

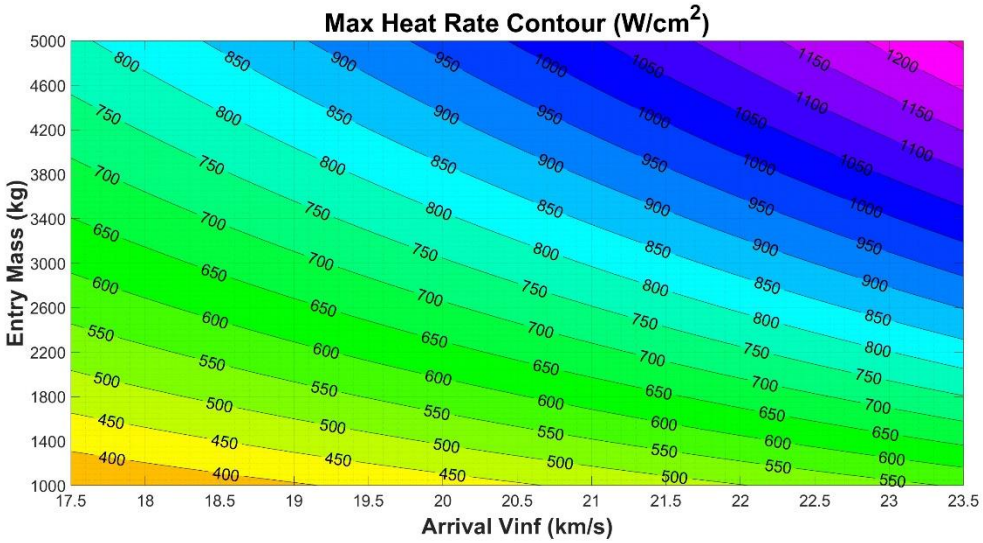

Figure 3. Heat Rate contour for BAM.

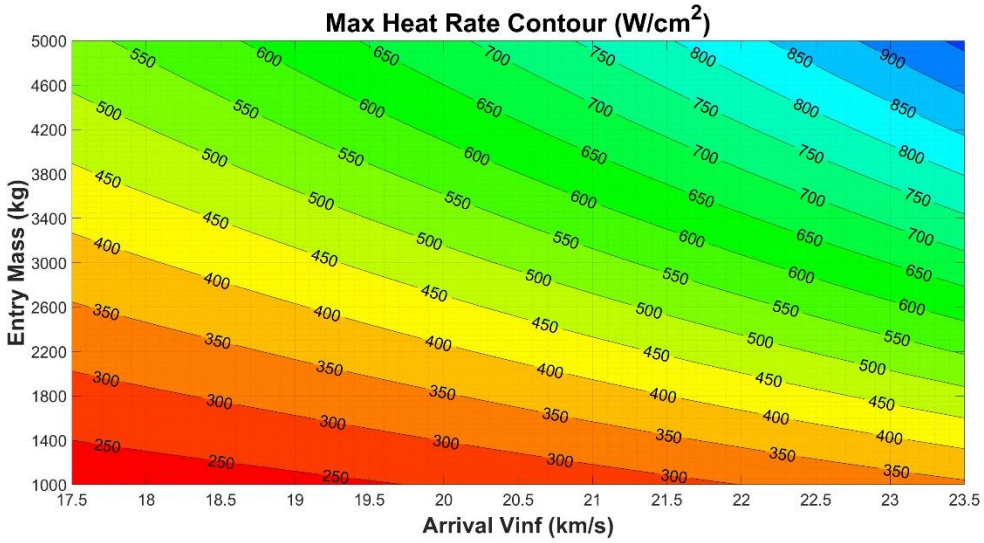

Figure 4. Heat Rate contour for MHD.

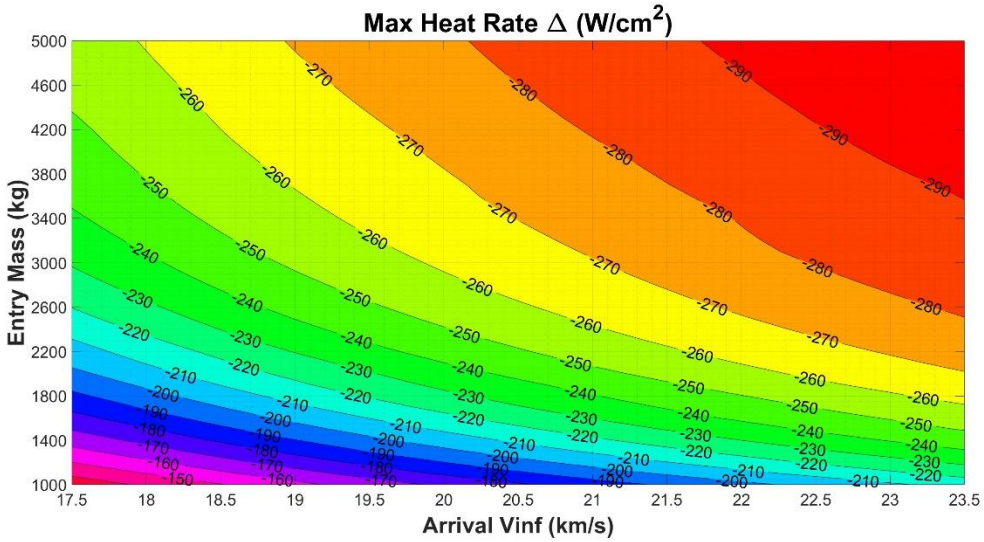

Figure 5. Relative contour showing the difference between MHD and BAM Heat Rates.

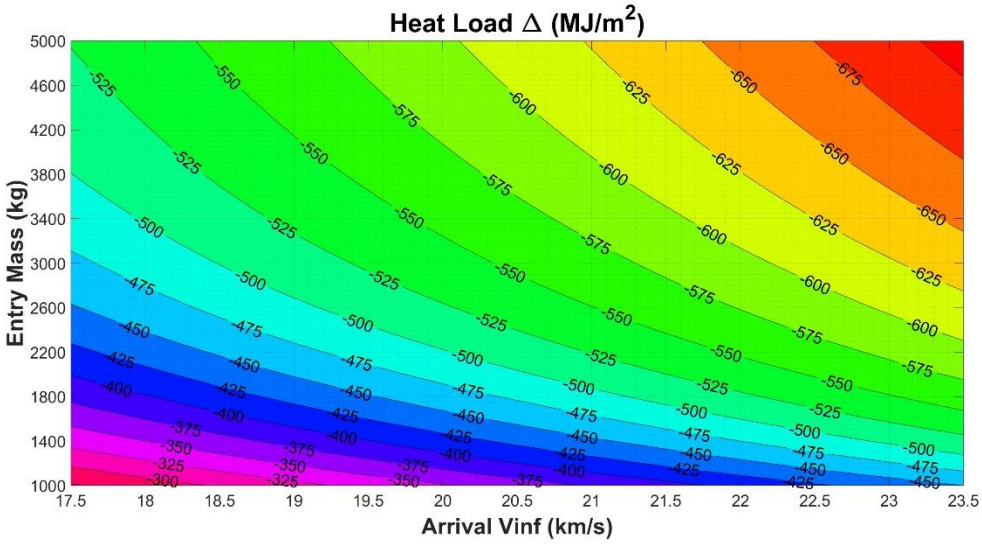

Figure 6. Relative contour showing the difference between MHD and BAM Heat Load.

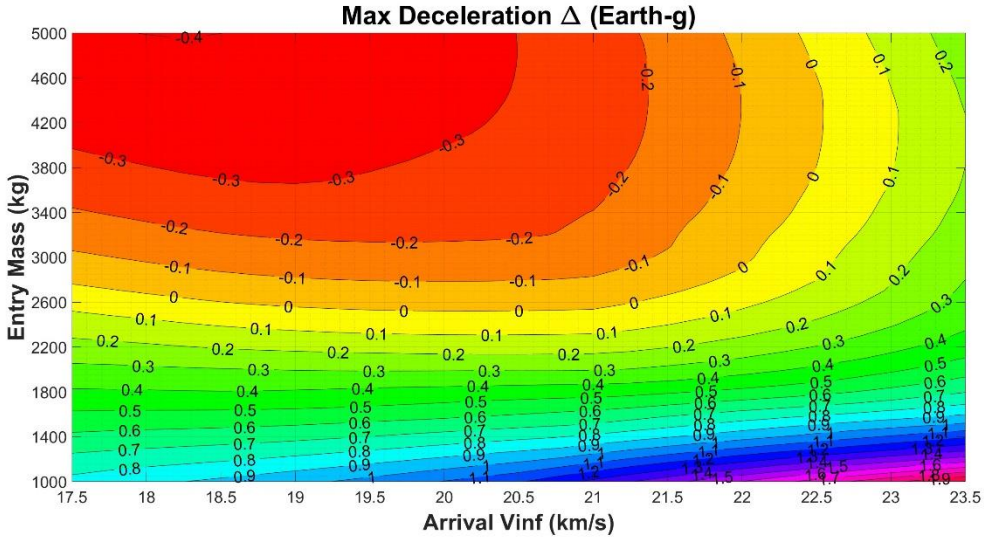

Figure 7. Relative contour showing the difference between MHD and BAM Maximum Deceleration.

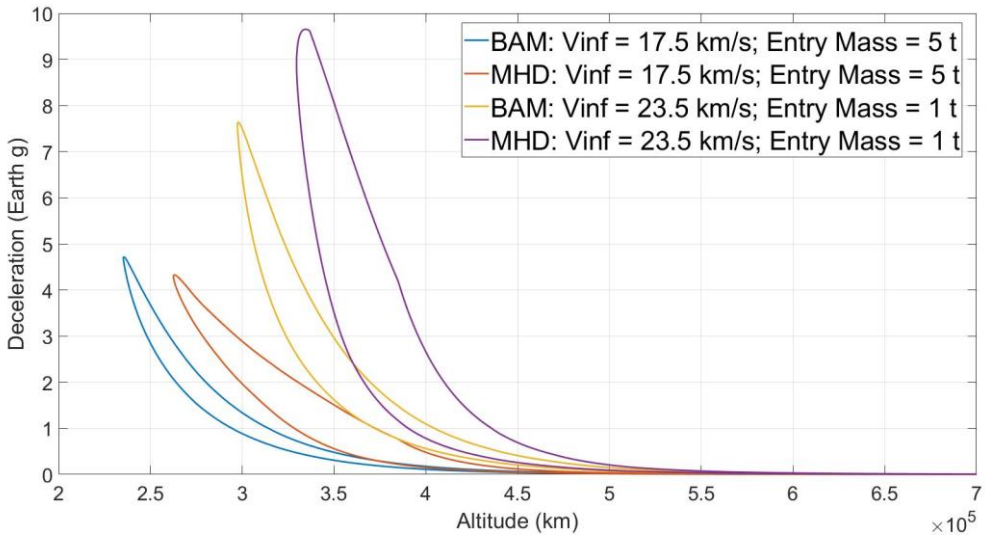

Figure 8. Deceleration versus Altitude comparing MHD and BAM at the extreme corners of the Maximum Deceleration contour in Figure 7.

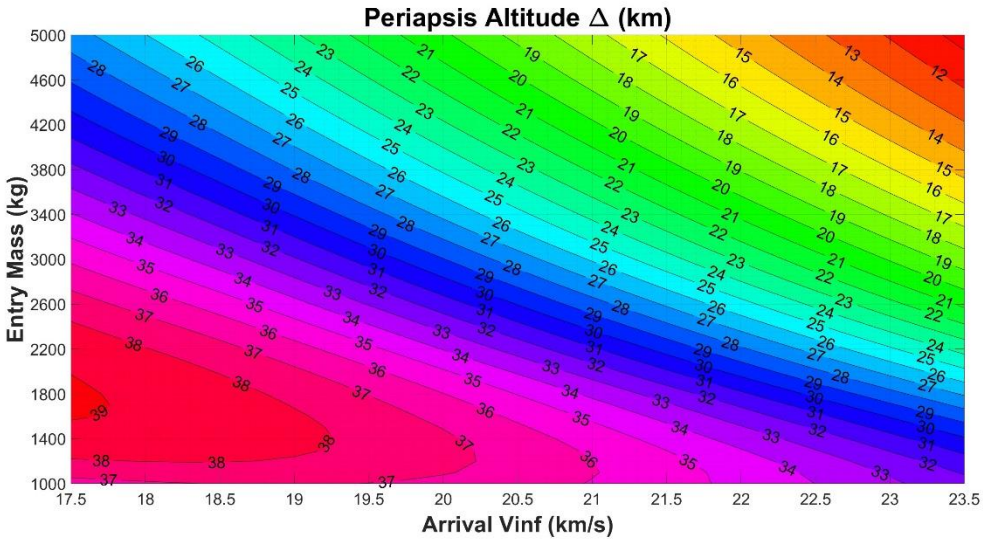

Figure 9. Relative contour showing the difference between MHD and BAM Periapsis Altitude.

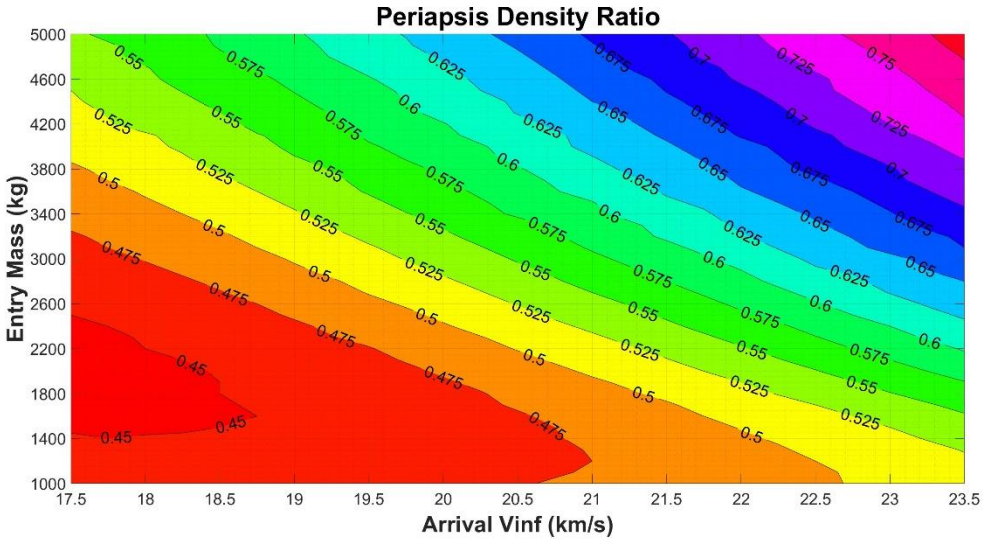

Figure 10. Relative contour showing the ratio of MHD to BAM Periapsis Density.

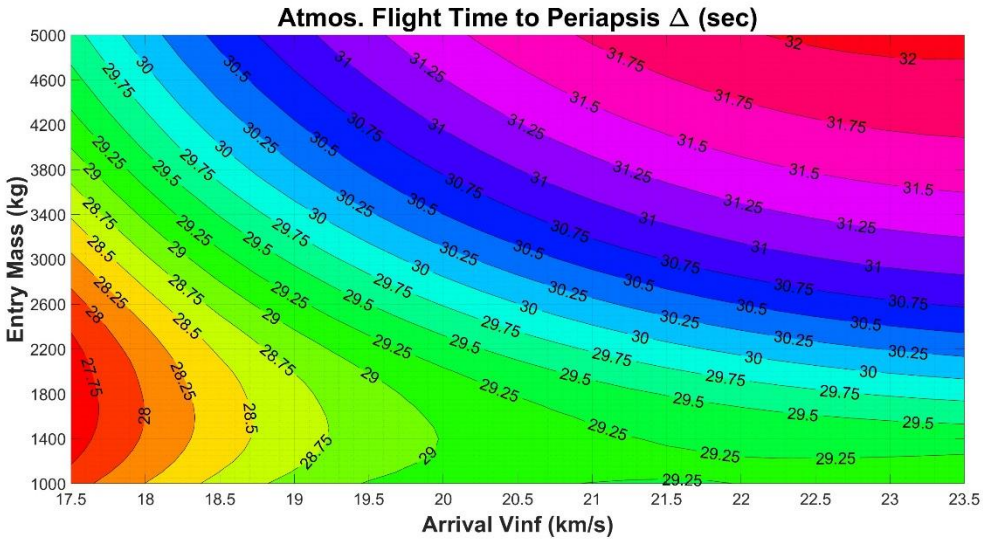

Figure 11. Relative contour showing the difference between MHD and BAM Flight Time to Periapsis.

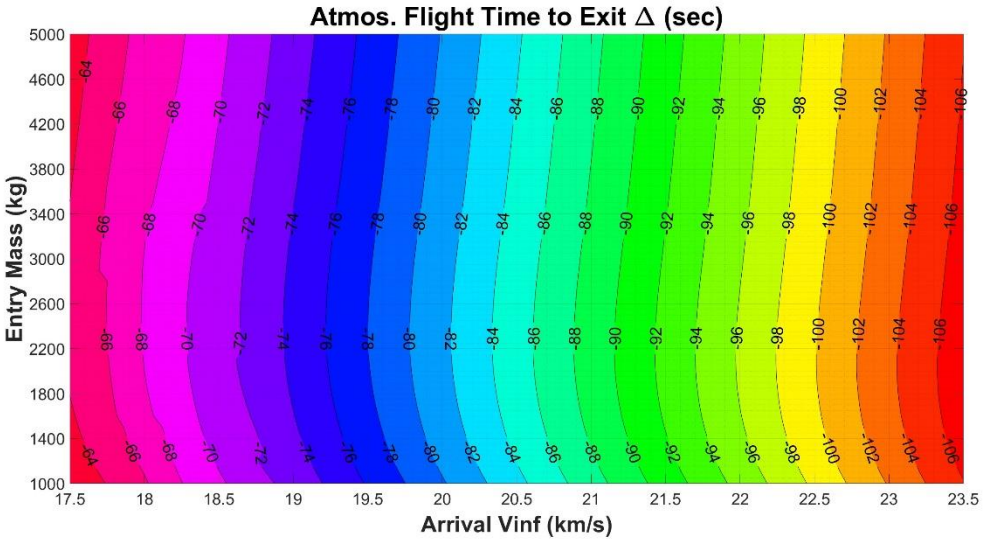

Figure 12. Relative contour showing the difference between MHD and BAM Total Atmospheric Flight Time.

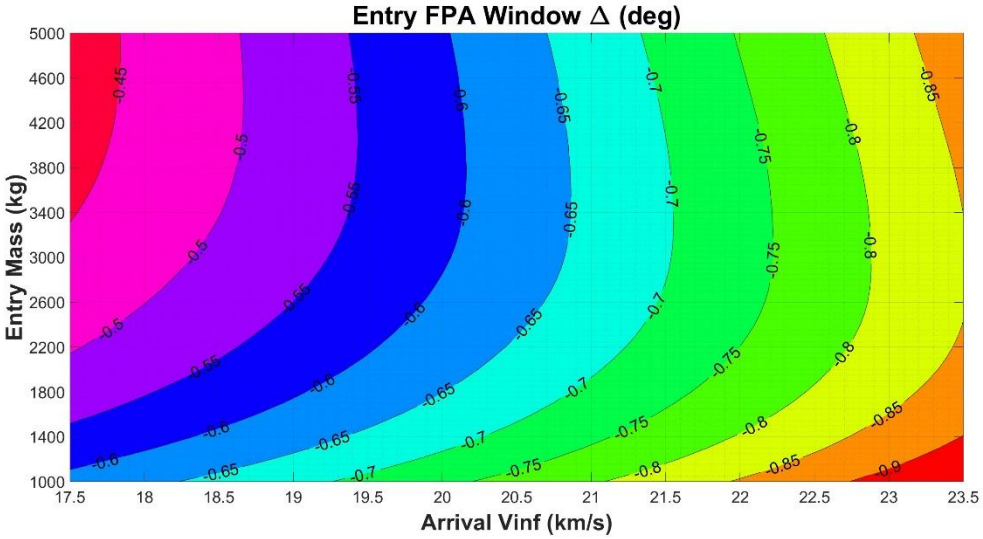

Figure 13. Relative contour showing the difference between MHD and BAM Entry Flight Path Angle Window.

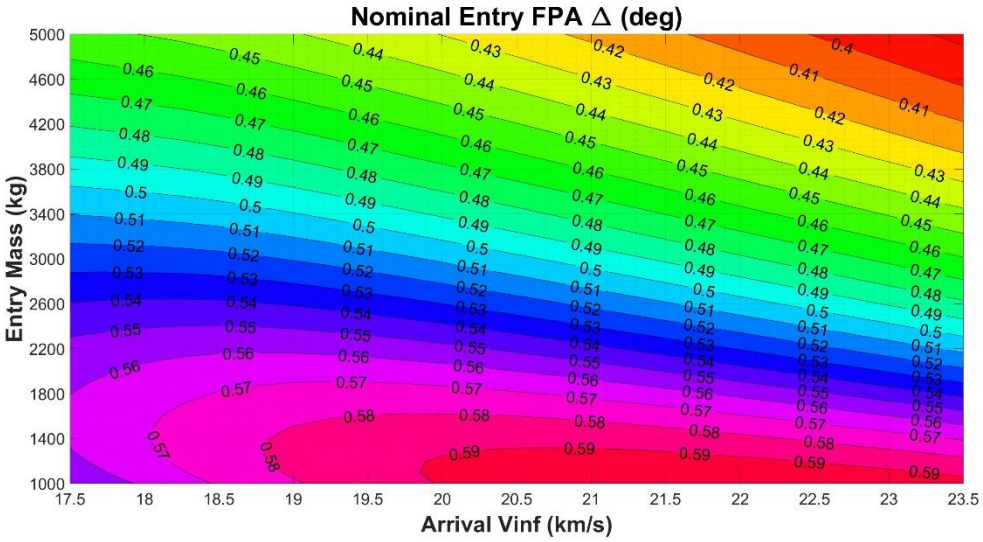

Figure 14. Relative contour showing the difference between MHD and BAM Entry Flight Path Angle.

Aeroheating and TPS Sizing Analysis. To illustrate the potential mass savings for MHD cases, additional aeroheating and TPS sizing analyses were performed to quantify the heating environment and TPS mass for a select set of trajectory cases.

Initial aeroheating and TPS sizing analyses were performed at Vinf = 17.5 km/s and covered an entry mass range from 1 t up to 20 t to investigate the impact of ballistic coefficient on the relative performance of MHD. Additional cases at Vinf = 20.5 km/s and Vinf = 23.5 km/s were added to investigate the influence of entry velocity on the relative performance of MHD. These cases covered an entry mass range of 3 t to 10 t.

Note that for the MSL capsule with a fixed 4.57 m diameter, the higher range of masses may not be technically feasible. However, these entry masses were assessed to illustrate the impact that higher ballistic coefficients have on both BAM and MHD cases. The resulting trends are expected to hold for other configurations (such as mid-L/D shape) that can accommodate significantly larger payload masses within their outer mold lines and operate effectively at these higher ballistic coefficients.

Analysis results are captured in Table 2 and Figure 15. Table 2 shows the maximum convective, radiative, and total heat rate along with the trajectory-integrated total heat load for the cases assessed. Figure 15 is a stacked bar chart illustrating the TPS sizing results for the cases assessed.

As shown in Table 2 and as discussed in the *Relative Flight Performance Assessment* results subsection above, MHD has appreciably lower maximum (convective, radiative, and total) heat rates and total heat load relative to the corresponding BAM aerodynamic-only cases. The heating profiles for each of these cases was then used to size the appropriate TPS material concept (based on the maximum total heat rate) for each.

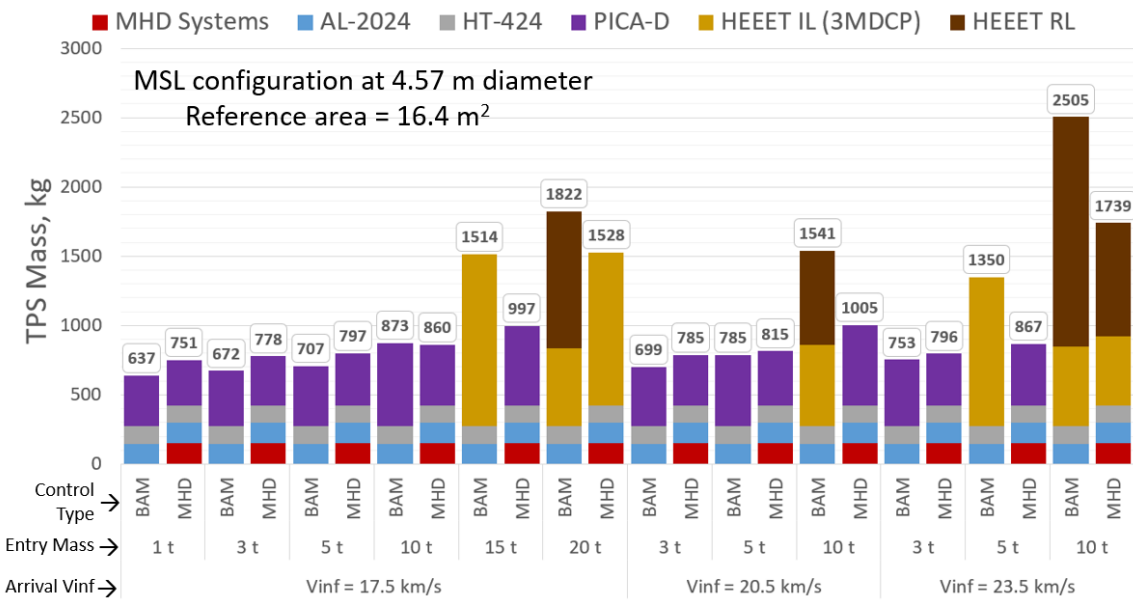

Figure 15. TPS Sizing Comparison for BAM and MHD over a range of Arrival Masses and Velocities.

From Figure 15, for the lower entry masses (i.e., ballistic coefficients) at a given Vinf, we see the MHD case has a slightly lower mass of TPS, but when the cost of the MHD system mass is included, the BAM case is preferred. As entry mass increases, however, the relative benefit of MHD increases and the results begin to favor the MHD cases, especially when the heat rates for BAM begin to exceed the capability of PICA-D, requiring the BAM case to utilize one of the HEEET variants. At the high end of the assessed entry mass cases, for all velocities assessed, we observe significant mass advantage for MHD, even for cases where both BAM and MHD require the use of HEEET.

The clear takeaway from Figure 15 is that at higher entry masses (i.e., ballistic coefficients) the MHD cases may stay under the PICA maximum heat rate threshold while the corresponding BAM cases cannot. This results in substantial benefit for MHD, and that benefit increases as the entry mass increases.

DISCUSSION AND FINDINGS

The contour plots above provide a wide envelope for an initial investigation of MHD drag augmented spacecraft compared to an aerodynamic-only BAM controlled spacecraft. From these three key findings can be drawn, which motivate future investigations.

1) The introduction of MHD drag technology reduces the aerothermal environment (see Figure 5 and Figure 6). The increased deceleration (see Figure 7 and Figure 8) at higher altitudes enables a shallower dive into the Neptunian atmosphere (see Figure 14), thus reducing the overall atmospheric densities the MHD drag augmented spacecraft experiences (see Figure 10).

A second point regarding the shallower dive can be made in comparing discrete points along the trajectories of MHD drag augmented and BAM spacecraft. In comparing density points common between the two systems, the MHD drag augmented spacecraft has a slower velocity, thus further reducing the convective and radiative heat fluxes.

Table 2. Heat Rate and Heat Load Comparison for BAM and MHD Cases.

Arrival Vinf (km/s)	Entry Mass (t)	Option	Max Convective Heat Rate (W/cm^2)	Max Radiative Heat Rate (W/cm^2)	Max Total Heat Rate (W/cm^2)	Total Heat Load (MJ/m^2)
17.5	1	BAM	350	28	378	719
		MHD	216	7	223	427
	3	BAM	609	136	745	1319
		MHD	378	34	412	756
	5	BAM	790	290	1080	1798
		MHD	535	92	627	1099
	10	BAM	1131	824	1955	2878
		MHD	856	355	1211	1913
	15	BAM	1401	1546	2947	3933
		MHD	1111	757	1868	2704
	20	BAM	1626	2397	4023	5010
		MHD	1330	1281	2611	3503
20.5	3	BAM	774	326	1100	1719
		MHD	508	96	604	977
	5	BAM	1005	692	1697	2428
		MHD	723	261	984	1479
	10	BAM	1440	1968	3408	4158
		MHD	1140	965	2105	2736
23.5	3	BAM	970	642	1612	2224
		MHD	684	230	914	1275
	5	BAM	1259	1386	2645	3270
		MHD	962	621	1583	2004
	10	BAM	1805	4047	5852	6032
		MHD	1499	2280	3779	3985

2) The introduction of MHD drag provides TPS mass savings and these savings increase for larger spacecraft (see Figure 15). In looking at all the trades together, the lower heat flux reduces the amount of TPS lost due to ablation. The lower heat loads (see Figure 6 and Table 2) reduce the amount of TPS material required for insulation. This reduction is due to both the reduced heat fluxes and the overall reduction in flight times (from atmospheric entry to exit) by tens of seconds (see Figure 12).

3) The MHD drag augmented spacecraft has a smaller entry flight path angle window (see Figure 13). The MHD drag augmentation does not offer increased flexibility in targeting a desired orbit as compared to BAM. This finding coincides with past work in aerodynamic drag only aerocapture[17]. The controllability offered through lift modulation[40] (as achieved through BAM),

increases the orbit targeting capabilities of the spacecraft. Therefore, this finding speaks more to the limitation of drag augmentation than to the limitations of MHD force generation itself. Future work is needed to investigate the impacts of MHD lift augmented control.

Higher L/D ratios can be achieved by adopting a mid-L/D vehicle shape. Figure 16 provides an example of a mid-L/D shape. These forebody shapes are more slender than blunt bodies, which leads to higher ballistic coefficients yielding higher heat loads and heating rates, resulting in larger TPS mass. Theoretically, and as analyzed by Moses[10] and Parent[11], MHD can also be applied to mid-L/D vehicle concepts. As shown in Figure 17, a location on the mid-L/D shape was selected just outside the stagnation region, where the flow is still sufficiently conductive electrically and thermally to produce Lorentz forces in the presence of a magnetic field.

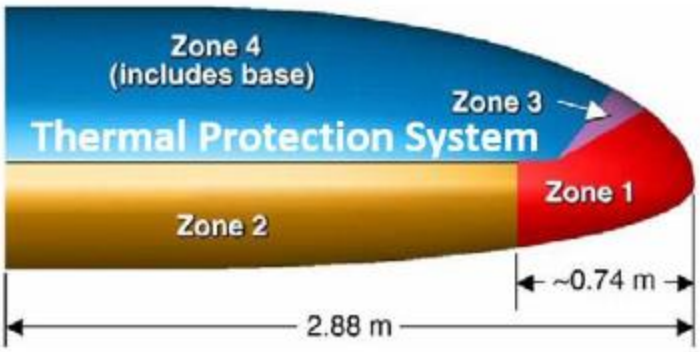

Figure 16. Vehicle Details for a Mid-Lift-to-Drag Ratio Concept (Courtesy of Lockwood, 2004)[41].

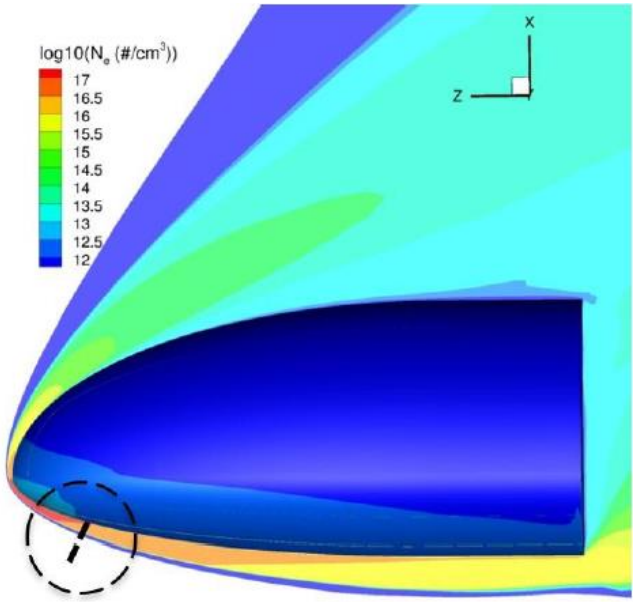

Figure 17. Electron Number Densities for a Neptune Entry of a Mid-Lift-to-Drag Ratio Vehicle Concept with the Location of the MHD Patch Identified by the Dashed Line.[10]

CONCLUSION

This work provides initial investigation into the impacts of MHD drag augmentation for aerocapture at Neptune. A wide range of entry masses (i.e., ballistic coefficients) were investigated to demonstrate the benefits of MHD to both small probe class vehicles and to larger single-stage reusable landing vehicles. The investigations into arrival Vinf demonstrate the possibilities of MHD drag augmentation for use in decreasing the interplanetary transit time. Over all the trades, MHD drag augmentation shows promise in reducing the aerothermal requirements on TPS. This can be utilized to reduce the overall spacecraft mass, increase payload, and/or increase the arrival Vinf (thus decreasing the interplanetary transit time).

There are two major limitations in this work that warrant future development and study. First, control forces, regardless of them being aerodynamic or MHD, can be employed for drag modulation, lift modulation, or direct force control. Past work in aerodynamic-based entry control has shown the limitations of drag modulation as compared to lift and direct force control.[17] The use of MHD drag modulation was employed here due to the resources available and ease of implementation. However, even with this limitation, MHD drag modulation did provide favorable results compared to aerodynamic-only BAM. It is expected that further gains can be had through MHD-powered lift modulation and DFC, which will be the focus of future investigations. Second, this investigation uses open-loop control, which limits the results to nominal conditions. Future closed-loop control investigations are needed to demonstrate the capability of added MHD control forces for mitigating uncertainties, such as delivery errors, atmospheric perturbations, and navigation errors. Even with these limitations, this work showcases the promise of MHD control forces for a wide trade space and motivates further investigations into MHD guidance and control.

ACKNOWLEDGMENTS

The authors would like to think the following:

- Dr. Thomas West, NASA Langley Research Center, Vehicle Analysis Branch for supporting the aerothermal analysis and modeling.
- Dr. Soumyo Dutta and Dr. Rohan Deshmukh, NASA Langley Research Center, Atmospheric Flight and Entry Systems Branch, for their technical insights, guidance, and support for this effort.
- Danny Nguyen and Dr. Hisham Ali, University of Colorado Boulder, for their trajectory simulation development work, which this work is derived from, and for their consultation work on MHD and magnet design.
- The NASA Langley Research Center Innovation Fund – Internal Research and Development Program for their financial support.

REFERENCES

[1] Resler, E. and Sears, W., "The Prospects for Magneto-Aerodynamics," *Journal of Aerospace Sciences*, Vol. 4, No. 4, pp. 235-258, 1958.

[2] Ziemer, R. and Bush, W., "Magnetic Field Effects on Bow Shock Stand-Off Distance," *Phys. Rev. Lett.* Vol. 1, No. 2, pp. 58-59, 1958.

[3] Moses, R., "Plasma Assisted ISRU at Mars," 15th International Conference on MHD Energy Conversion, Vol. 2, 2005, pp. 468–477.

[4] Moses, R., "Regenerative Aerobraking," AIP Conference Proceedings, Vol. 746, 2005, pp. 1361–1370.

[5] Fujino, T., Yoshino, T., and Ishikawa, M., "Numerical Analysis of Reentry Trajectory Coupled with Magnetohydrodynamics Flow Control," *Journal of Spacecraft & Rockets*, Vol. 45, No. 5, pp. 911–920, 2008. https://doi.org/10.2514/1.33385

[6] Fujino, T. and Ishikawa, M., "Feasibility of an Onboard Surface Hall Magnetohydrodynamic Power Generator in Reentry Flight," *Journal of Propulsion & Power*, Vol. 25, No. 1, pp. 83–93, 2009. https://doi.org/10.2514/1.33354

[7] Kim, M. and Boyd, I., "Effectiveness of a Magnetohydrodynamics System for Mars Entry," *Journal of Spacecraft & Rockets*, Vol. 49, No. 6, pp. 1141–1149, 2012. https://doi.org/10.2514/1.A32256

[8] Ali, H. and Braun, R., "Modeling Magnetohydrodynamic Energy Generation and Storage in Planetary Entry System Conceptual Design," *Journal of Spacecraft & Rockets*., Vol. 55, No. 2, pp. 356–364, 2018. https://doi.org/10.2514/1.A33948

[9] Ali, H., "Magnetohydrodynamic Energy Generation and Flow Control for Planetary Entry Vehicles," Georgia Institute of Technology, 2019.

[10] Moses, R., Cheatwood, F., Johnston, C., Macheret, S., Parent, B., Little, J., Williams, R., Green, J., Austin, M., and Aldrin, A., "New MHD Lift Concept for More Efficient Missions to Mars and Neptune," AIAA SCITECH 2022 Forum, January 3-7, 2022, San Diego, CA & Virtual, https://doi.org/10.2514/6.2022-0934

[11] Parent, B., Rajendran, P., Moses, R., Johnston, C., Cheatwood, F., Macheret, S., and Little, J., "Effect of Plasma Sheaths on Earth Re-entry MHD Processes," AIAA 2022-0980, AIAA SCITECH 2022 Forum, January 3-7, 2022, San Diego, CA & Virtual, https://doi.org/10.2514/6.2022-0980

[12] Parent, B., Fuentes, F., and LaFoley, S., "Two-Electrode vs Electrode-less MHD-Enhanced Aerocapture," AIAA 2024-1649, AIAA SCITECH 2024 Forum, 8-12 January 2024, Orlando, FL, https://doi.org/10.2514/6.2024-1649

[13] Nguyen, D., Dutta, S., Moses, R, Ali, H., and Gunter, B., "Feasibility and Performance Analysis of Magnetohydrodynamic Control for Aerocapture at Neptune," No. AAS 22-803, AAS/AIAA Astrodynamics Specialist Conference, August 7-11, 2022, Charlotte, North Carolina.

[14] Nguyen, D., "Performance Analysis of Magnetohydrodynamic (MHD) Drag Modulation for Actively Controlled Aerocapture at Neptune," IPPW 2024, 21st International Planetary Probe Workshop, June 8th - 14th, Williamsburg, Virginia.

[15] Fawley, D., Putnam, Z., D'Souza, S., McDaniel, R., and Borner A., "Aerodynamic Assessment of a 70 deg Spherecone at 0 deg Angle of Attack Flying Hypersonically in the Mars Atmosphere," AIAA-2024-1822, AIAA SCITECH 2024 Forum, January 8-12, 2024, Orlando, FL, https://doi.org/10.2514/6.2024-1822

[16] Deshmukh, R., Spencer, D., and Dutta, S., "Investigation of Direct Force Control for Aerocapture at Neptune," *Acta Astronautica*, Vol. 175, pp. 375-386, 2020, https://doi.org/10.1016/j.actaastro.2020.05.047

[17] Deshmukh, R., Spencer, D., and Dutta, S., "Flight Control Methodologies for Neptune Aerocapture Trajectories," *Acta Astronautica*, Vol. 193, pp. 255-268, 2022, https://doi.org/10.1016/j.actaastro.2022.01.004

[18] Meyer, R., "On Reducing Aerodynamic Heat-Transfer Rates by Magnetohydrodynamic Techniques," *Journal of Aerospace Sciences*, Vol. 25, No. 9, pp. 561–566, 1958. https://doi.org/10.2514/8.7781

[19] Poggie, J. and Gaitonde, D., "Magnetic Control of Hypersonic Blunt Body Flow," AIAA 2000-0452, 38th Aerospace Sciences Meeting and Exhibit, 10 January 2000 - 13 January 2000, Reno, NV, USA, https://doi.org/10.2514/6.2000-452

[20] Macheret, S., Shneider, M., Candler G., Moses, R., and Kline, J., "Magnetohydrodynamic Power Generation for Planetary Entry Vehicles," AIAA-2004-2560, 35th AIAA Plasmadynamics and Lasers Conference, June 28, 2004 – July 1, 2004, https://doi.org/10.2514/6.2004-2560

[21] Gülhan, A., Esser, B., Koch, U., Siebe, F., Riehmer, J., Giordano D., and Konigorski, D., "Experimental Verification of Heat-Flux Mitigation by Electromagnetic Fields in Partially-Ionized-Argon Flows," *Journal of Spacecraft & Rockets*, Vol. 46, No. 2, pp. 274–283, 2009. https://doi.org/10.2514/1.39256

[22] Kawamura, M., Matsuda, A., Katsurayama, H., Otsu, H., Konigorski, D., Sato, S., and Abe, T., "Experiment on Drag Enhancement for a Blunt Body with Electrodynamic Heat Shield," *Journal of Spacecraft and Rockets*, Vol. 46, No. 6, pp. 1171–1177, 2009. https://doi.org/10.2514/1.44230

[23] Bisek, N., "Numerical Study of Plasma-Assisted Aerodynamic Control for Hypersonic Vehicles," The University of Michigan, 2010.

[24] Kawamura, M., Nagata, Y., Katsurayama, H., Otsu, H., Yamada, K., and Abe, T., "Magnetoaerodynamic Force on a Magnetized Body in a Partially Ionized Flow," *Journal of Spacecraft & Rockets*, Vol. 50, No. 2, pp. 347–351, 2013. https://doi.org/10.2514/1.A32279

[25] Gildfind, D., Jacobs, P., Gollan, R., Toniato, P., McIntyre, T., Andrianatos, A., James, C., and Morgan, R., "Flow Characterization and Modeling of the X2 and X3 Expansion Tubes," Centre for Hypersonics, University of Queensland, Australia, November 11, 2018.

[26] Smith, D., Gildfind, D., Jacobs, P., Cullen, T., James, C., Liu, Y., Gollan, R., and McIntyre, T., "Magnetohydrodynamic Drag Measurements in an Expansion Tunnel with Argon Test Gas," *AIAA Journal*, Vol. 58, No. 10, pp. 4495–4504, 2020. https://doi.org/10.2514/1.J059540

[27] Gildfind, D., Smith, D., Lefevre, A., Jacobs, P., and McIntyre, T., "Magnetohydrodynamic Aerobraking Shock Stand-Off Measurements with Flight Representative Electrodynamic Boundary Conditions," *AIAA Journal*, Vol. 60, No. 1, pp. 41–55, 2022. https://doi.org/10.2514/1.J060466

[28] Noca, M. and Bailey, R., "Mission Trades for Aerocapture at Neptune," AIAA 2004-3843, 40th AIAA/ASME/SAE/ASEE Joint Propulsion Conference and Exhibit, July 11-14, 2004, Fort Lauderdale, FL. https://doi.org/10.2514/6.2004-3843

[29] Thompson, K., Johnston, C., Hollis, B., and Lessard, V., "Recent Improvements to the LAURA and HARA Codes," AIAA-2020-3030, AIAA Aviation 2020 Forum, June 15-19, 2020, https://doi.org/10.2514/6.2020-3030

[30] Parent, B., Shneider, M., and Macheret, S., "Detailed Modeling of Plasmas for Computational Aerodynamics," *AIAA Journal*, Vol. 54, No. 3, pp. 898–911, 2016, https://doi.org/10.2514/1.J054624

[31] Sutton, K., and Graves, R., "A General Stagnation Point Convective Heating Equation for Arbitrary Gas Mixtures," NASA TR R-376, November 1971.

[32] Lugo, R., Shidner, J., Powell, R., Marsh, S., Hoffman, J., Litton, D., and Schmitt, T., "Launch Vehicle Ascent Trajectory Simulation Using the Program to Optimize Simulated Trajectories II (POST2)," AAS-17-274, AAS/AIAA Space Flight Mechanics Conference, February 5, 2017.

[33] Milos, F. and Chen, Y., "Ablation, Thermal Response, and Chemistry Program for Analysis of Thermal Protection Systems," *Journal of Spacecraft & Rockets*, Vol. 50, No. 1, pp. 137-149, 2013, https://doi.org/10.2514/1.A32302

[34] Mahzari, M., Beck, R., Hwang, H., Monk, J., Morgan, J., Williams, J., and Edquist, K., "Development and Sizing of the Mars 2020 Thermal Protection System," AIAA 2022-3951, AIAA Aviation Forum, June 2022, https://doi.org/10.2514/6.2022-3951

[35] Milos, F., Gasch, M., and Prabhu, D., "Conformal Phenolic Impregnated Carbon Ablator Arcjet Testing, Ablation, and Thermal Response," *Journal of Spacecraft & Rockets*, Vol. 52, No. 3, pp. 804–812, 2015, https://doi.org/10.2514/1.A33216

[36] Milos, F., Chen, Y., and Mahzari, M., "Arcjet Tests and Thermal Response Analysis for Dual-Layer Woven Carbon Phenolic," *Journal of Spacecraft & Rockets*, Vol. 55, No. 3, pp. 712–722, 2018, https://doi.org/10.2514/1.A34142

[37] Venkatapathy, E., Prahbu, D., Allen, G., Milos, F., and Gasch, M., "Next Generation Thermal Protection Systems for Outer Planet Missions," Poster presented virtually at the Outer Planets Assessment Group (OPAG) Meeting, August 30, 2021, https://ntrs.nasa.gov/citations/20210020896

[38] Prahbu, D., "Exploration of the Viability of HEEET as a TPS for Saturn, Neptune, and Uranus Entries," Outer Planets Assessment Group (OPAG) Meeting, September 11-12, 2018.

[39] Mahzari, M. and Milos, F., "Sizing and Margin Methodology for Dual-Layer Thermal Protection Systems," IPPW 2018, 15th International Planetary Probe Workshop, June 11th - 15th, Boulder, Colorado.

[40] Moses, R., "System and Method for Lift Augmentation of Atmospheric Entry Vehicles During Aerocapture and Entry, Descent, and Landing Maneuvers," U.S. Patent No: 12 125 636, October 22, 2024.

[41] Lockwood, M., "Neptune Aerocapture Systems Analysis," AIAA 2004-4951, AIAA Atmospheric Flight Mechanics Conference and Exhibit, August 16-19, 2004, Providence, Rhode Island, https://doi.org/10.2514/6.2004-4951